

Low-threshold lasing with a stationary inflection point in a three-coupled-waveguide structureKessem Zamir-Abramovich ^{1,*} Nathaniel Furman ² Albert Herrero-Parareda ²
Filippo Capolino ² and Jacob Scheuer ^{1,†}¹*School of Electrical Engineering, Tel-Aviv University, Tel-Aviv, Israel*²*Department of Electrical Engineering and Computer Science, University of California, Irvine, California 92697, USA*

(Received 13 August 2023; accepted 1 November 2023; published 5 December 2023)

The frozen mode regime is a unique slow-light scenario in periodic structures, where the flat bands (zero group velocity) are associated with the formation of high-order stationary points (also known as exceptional points). The formation of exceptional points is accompanied by enhancement of various optical properties such as gain, Q factor, and absorption, which are key properties for the realization of a wide variety of devices such as switches, modulators, and lasers. Here we present and study an integrated optical periodic structure consisting of three waveguides coupled via microcavities and a directional coupler. We study this design theoretically, demonstrating that a proper choice of parameters yields a third-order stationary inflection point (SIP). We also show that the structure can be designed to exhibit two almost overlapping SIPs at the center of the Brillouin zone. We study the transmission and reflection of light propagating through realistic devices composed of a finite number of unit cells and investigate their spectral properties in the vicinity of the stationary points. Finally, we analyze the lasing frequencies and threshold level of a finite structure (as a function of the number of unit cells) and show that it outperforms conventional lasers utilizing regular band-edge lasing (such as distributed-feedback lasers).

DOI: [10.1103/PhysRevA.108.063504](https://doi.org/10.1103/PhysRevA.108.063504)**I. INTRODUCTION**

Optical structures operating in the slow-light regime exhibit group velocities that are substantially lower than the speed of light in vacuum. These optical structures exhibit numerous interesting properties; hence, they are highly attractive for many applications. In particular, such structures have been found to exhibit enhancement of properties such as gain, absorption, and quality factor (Q factor) [1–5]. The frozen mode regime is a special case of slow light, which describes a solution of Bloch wave points with zero-group-velocity points (stopped light); this point is an outcome of the coalescence of Bloch waves (both eigenvalues and eigenvectors) at a single frequency. The points are called stationary points (or exceptional points [6]), and they appear in various types. These types differ in their dispersion properties (the relation between the k vector and the angular frequency ω) in the vicinity of these points [7].

In particular, there is a distinct difference between stationary points corresponding to the coalescence of an even and an odd number of modes. The latter are called stationary inflection points (SIPs). The lowest order of this class corresponds to the coalescence of three eigenvalues, and they are characterized by a cubic dispersion relation:

$$\omega - \omega_{\text{SIP}} \propto (k - k_{\text{SIP}})^3. \quad (1)$$

Compared to stationary points with a coalescence of an even number of eigenvalues and eigenvectors, SIPs exhibit several unique properties. More specifically, SIPs are not formed at the band edge, but rather within the Brillouin zone (BZ). Since SIPs correspond to the coalescence of three Bloch waves propagating in the *same* direction, they do not form a standing wave. This property renders SIPs interesting scientifically, as well as attractive for various applications involving slow and stopped light. For example, coupling light into and out of an optical structure supporting an SIP is more efficient, as the excitation of counterpropagating modes can be eliminated [8]. This is because in the vicinity of the SIP frequency, the k vector preserves its sign. As a result, counterpropagating waves can be suppressed, contrary to what occurs for stationary points of even order, such as degenerated band edges (DBEs). Moreover, the slow light regime helps match a slowly propagating mode to a fast mode across the interface of the structure [9]. Furthermore, the SIP resonance has been shown to be remarkably robust to structural disorder and perturbation [10]. In addition, SIPs have various applications such as noise-resilient sensors [11], ultrasensitive rotation sensors [12], broadband filters [13], broadband impedance matching [14], true time delay applications [15], and lasers [16].

There are many ways to generate stationary points [17–19], one of them being the use of optical periodic structures. In particular, previous studies have presented several periodic structures supporting SIPs, such as waveguides with multiple gratings [9,20], coupled resonators optical waveguides, [6], three-way periodic microstrip coupled waveguides [21], asymmetric serpentine optical waveguides [22], and coupled transmission lines for traveling wave tubes [23]. In

*kessemzamir@mail.tau.ac.il

†kobys@tauex.tau.ac.il

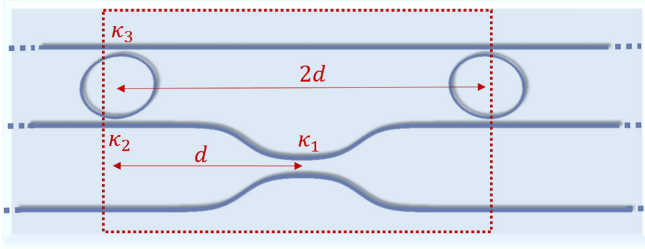


FIG. 1. Three periodic waveguides coupled with a ring resonator and directional coupler structure. The boundaries of the unit cell are marked by a dashed red line.

addition, previous studies have investigated lasers operating in the frozen mode and stopped light regimes. Lasers operating at a regular band edge (RBE), such as distributed-feedback lasers, have been investigated thoroughly. A laser operating at a DBE was investigated in Ref. [24]. There is a limited amount of research on lasers utilizing odd-order stationary points. In Ref. [25], the theory of unidirectional lasers operating in the frozen mode regime has been proposed and studied theoretically. The laser was designed to lase in the vicinity of an SIP, where nonreciprocity was introduced (by means of a magnetic layer) to obtain unidirectional lasing. More recently, an alternative structure, which also exhibits an SIP, was investigated theoretically as a potential laser near an SIP [16]. This structure, employing an asymmetric serpentine optical waveguide, was shown to exhibit a lower lasing threshold level than that of the same structure operating at an RBE instead.

In this paper, we propose and study an integrated, periodic structure that exhibits SIPs, and can be highly attractive for low-threshold laser applications. The structure consists of a repeating unit cell composed of three parallel waveguides coupled through a directional coupler and a ring resonator, as shown in Fig. 1. The central waveguide is coupled to the top waveguide with a ring resonator, and to the bottom one with a directional coupler. By properly setting the parameters of the structure—the resonator radius (R), the length of the unit cell ($2d$), and the power coupling coefficients of the coupler and the resonators (κ_1 , κ_2 , κ_3)—it is possible to obtain a dispersion relation exhibiting an SIP, and to control the properties of the structure. We show that this structure is versatile, in the sense that it can support SIPs at various frequencies, depending on the structure parameters. In contrast to many of the previously proposed structures (such as those presented in Ref. [22]), this structure's unit cell is robust and relatively simple to fabricate. It consists of simple and standard integrated optical elements, whose designed parameters can be readily adjusted and modified to tune the characteristics of the structure. We also perform a comprehensive analysis of the power transmission and reflection characteristics of this structure in two cases: (1) when all six input-output (IO) ports are available and (2) when only one input port and one transmission port are available. This is in contrast to previous studies that are only examined the latter case. In addition, we also analyze finite segments of the proposed structure when gain material is incorporated. We calculated the lasing threshold of this geometry, and found that the threshold gain

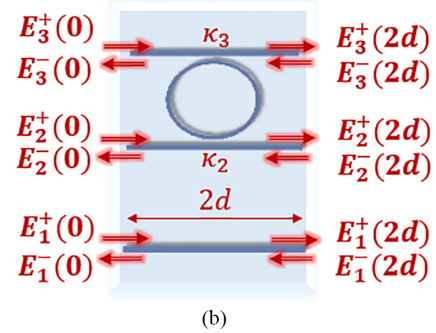
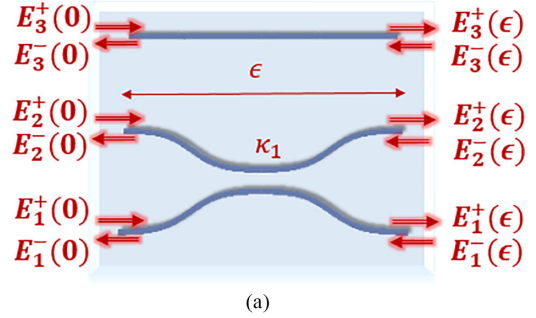


FIG. 2. The two sections of a unit cell: (a) the directional coupler and (b) the add-drop multiplexer of length $2d$

of our structure decreases proportionally to N^{-3} , where N is the number of unit cells. We learn that SIP-based devices outperform their RBE counterparts in terms of lasing threshold level. Our results regarding the properties of the threshold gain reinforce the results obtained in previous studies [16,25], especially in the context of SIP-based laser applications.

The rest of the paper is organized as follows: In Sec. II, we calculate the dispersion relation of the structure by finding a general analytic expression for the transfer matrix of a unit cell. The structure parameters are then optimized in order to obtain SIPs. In Sec. III, we numerically calculate the transmission and reflection for a finite structure. We discuss the spectral properties of the structure with three IO ports, and also with a single input and single transmission port. In Sec. IV we provide a brief analysis of the impact of fabrication imperfections on the spectral properties of a finite structure with three IO ports. We show some of the preliminary results, but the study will be continued in a separate paper. In Sec. V, we analyze an active version of this structure, incorporating optical gain material, and in Sec. VI we summarize the results and conclude. The time convention $e^{i\omega t}$ is used throughout the paper.

II. DISPERSION RELATION AND STATIONARY INFLECTION POINTS

We present the derivation of the unit-cell transfer matrix and obtain the dispersion relation of the eigenmodes in the infinitely long waveguiding structure. To calculate the Bloch wave-number dispersion relation of the structure shown in Fig. 1, we use the transfer-matrix method. For simplicity, we divide the unit cell into two sections: two coupled waveguides with a third separate waveguide seen in Fig. 2(a), and an

add-drop multiplexer (ADM) of length $2d$ seen in Fig. 2(b). Here we assume the coupling sections are infinitely small (e.g., point coupling, $\epsilon \rightarrow 0$).

$$\begin{bmatrix} E_1^+(\epsilon) \\ E_1^-(\epsilon) \\ E_2^+(\epsilon) \\ E_2^-(\epsilon) \\ E_3^+(\epsilon) \\ E_3^-(\epsilon) \end{bmatrix} = \begin{bmatrix} t_1 & 0 & r_1 & 0 & 0 & 0 \\ 0 & t_1 & 0 & -r_1 & 0 & 0 \\ 0 & 0 & t_1 & 0 & r_1 & 0 \\ 0 & 0 & 0 & t_1 & 0 & -r_1 \\ 0 & 0 & 0 & 0 & 1 & 0 \\ 0 & 0 & 0 & 0 & 0 & 1 \end{bmatrix} \begin{bmatrix} E_1^+(0) \\ E_1^-(0) \\ E_2^+(0) \\ E_2^-(0) \\ E_3^+(0) \\ E_3^-(0) \end{bmatrix} \quad (2)$$

where $t_1 \triangleq \sqrt{1 - \kappa_1}$ and $r_1 \triangleq -i\sqrt{\kappa_1}$. Here, κ_1 is the intensity coupling between the two waveguides. E_n is the electric-field phasor in the n th waveguide.

Similarly, the transfer matrix for the section of the add-drop multiplexer is written in Eq. (3), where $T_{1,2}$ and $D_{1,2}$ are the field transmission functions of the through and drop port of two ADMs. $T_{1,2}$ and $D_{1,2}$ are written in Eq. (4). Index 1 (T_1 , D_1) corresponds to an ADM with coupling coefficients κ_3 at the through port and κ_2 at the drop port. Index 2 (T_2 , D_2) corresponds to the opposite case of the ADM (κ_2 at the through port and κ_3 at the drop port):

$$\begin{bmatrix} E_1^+(2d) \\ E_1^-(2d) \\ E_2^+(2d) \\ E_2^-(2d) \\ E_3^+(2d) \\ E_3^-(2d) \end{bmatrix} = \begin{bmatrix} e^{-2i\phi} & 0 & 0 & 0 & 0 & 0 \\ 0 & e^{2i\phi} & 0 & 0 & 0 & 0 \\ 0 & 0 & (T_2 - \frac{D_1 D_2}{T_1})e^{-2i\phi} & 0 & 0 & \frac{D_1}{T_1} \\ 0 & 0 & 0 & \frac{1}{T_2}e^{2i\phi} & -\frac{D_1}{T_2} & 0 \\ 0 & 0 & 0 & \frac{D_2}{T_2} & (T_1 - \frac{D_1 D_2}{T_2})e^{-2i\phi} & 0 \\ 0 & 0 & -\frac{D_2}{T_1} & 0 & 0 & \frac{1}{T_1}e^{-2i\phi} \end{bmatrix} \begin{bmatrix} E_1^+(0) \\ E_1^-(0) \\ E_2^+(0) \\ E_2^-(0) \\ E_3^+(0) \\ E_3^-(0) \end{bmatrix}, \quad (3)$$

$$\begin{aligned} T_1 &= \frac{\sqrt{1 - \kappa_3} - \sqrt{(1 - \kappa_2)(1 - \alpha)}e^{-i\phi}}{1 - \sqrt{(1 - \kappa_3)(1 - \kappa_2)(1 - \alpha)}e^{-i\phi}}, & D_1 &= \frac{-\sqrt{\kappa_3 \kappa_2}(1 - \alpha)^{\frac{1}{4}}e^{-i\frac{\phi}{2}}}{1 - \sqrt{(1 - \kappa_3)(1 - \kappa_2)(1 - \alpha)}e^{-i\phi}}, \\ T_2 &= \frac{\sqrt{1 - \kappa_2} - \sqrt{(1 - \kappa_3)(1 - \alpha)}e^{-i\phi}}{1 - \sqrt{(1 - \kappa_2)(1 - \kappa_3)(1 - \alpha)}e^{-i\phi}}, & D_2 &= D_1. \end{aligned} \quad (4)$$

$\phi = k_0 n_w d$ and $\varphi = k_0 n_r 2\pi R$ are phase accumulations in a straight waveguide with length d and a ring resonator with radius R , respectively. n_w is the effective refractive index of the straight waveguide, and n_r is the effective refractive index of the curved ring waveguide. α represents intensity loss per revolution inside the resonator ring. For the dispersion relation analysis, we assume $\alpha = 0$. The complete transfer matrix of the unit cell, \mathbf{M} , is obtained by multiplying the matrices of the two sections. By invoking the Bloch theorem, the dispersion relation of the periodic structure is obtained from Eq. (5):

$$|\mathbf{M} - \mathbf{I}e^{-ik2d}| = 0 \quad (5)$$

where $||$ denotes the determinant operation, and \mathbf{I} is the 6×6 identity matrix.

A. Separated stationary inflection points

Equation (5) provides the foundation for analyzing the eigenmodes in the structure depicted in Fig. 1, leading to the dispersion relation of an infinitely long structure for a specific set of parameters ($d, R, \kappa_1, \kappa_2, \kappa_3$). Obtaining an SIP requires a specific choice of parameters. Figure 3(a) depicts

the magnitude of the determinant of the matrix $\mathbf{M} - \mathbf{I}e^{-ik2d}$ for the set of parameters: set 1 listed in Table I. The blue-green lines in the figure indicate magnitude close to zero, i.e., solutions of Eq. (5), thus indicating the $k - \omega$ dispersion relation. The red circles denote potential SIPs at $\lambda \approx 1.54 \mu\text{m}$, related to frequency $\omega_s = \frac{2\pi c}{\lambda}$. Note that two symmetric SIPs are obtained due to reciprocity. The inset in Fig. 3(a) shows a zoom-in on the right SIP. It can be seen that at this point we obtain $\frac{\partial \omega}{\partial k} = 0$, and a third-degree polynomial in its vicinity, which is indicative of a frozen mode regime. Nevertheless, this does not guarantee an SIP, as the coalescence of both eigenvalues and eigenvectors still needs to be verified.

Following the unit-cell separation, obtaining the transfer matrices for each section is straightforward. The transfer matrix for the three waveguides with a single directional coupler κ_1 is written in Eq. (2):

To verify that this is indeed a stationary point of order 3, we consider the eigenvalues of the transfer matrix \mathbf{M} . Any input field in this structure can be spanned by a basis of six propagating and evanescent waves which are the eigenvectors of \mathbf{M} . At a given frequency, the eigenvalues of \mathbf{M} are designated as $\{\gamma\}_{i=1}^6$, where the relation between the eigenvalues and the corresponding wave numbers k is given by Eq. (6):

$$\gamma = e^{-ik2d}. \quad (6)$$

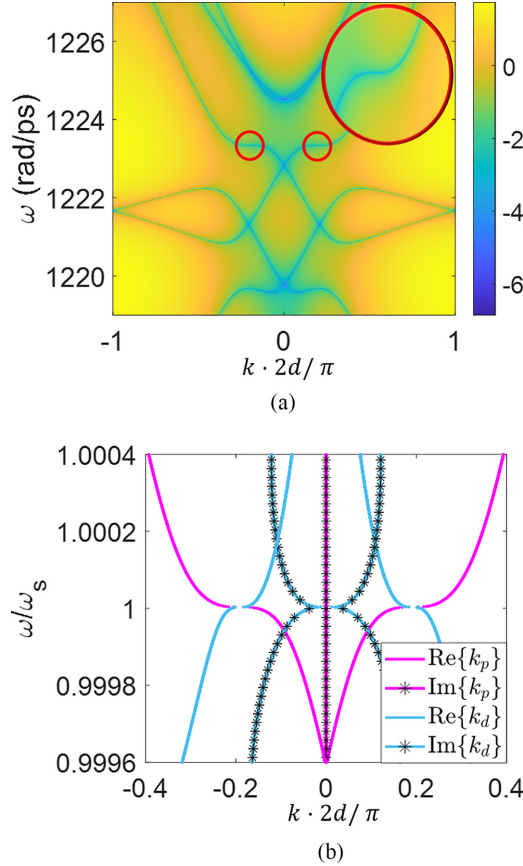


FIG. 3. Set 1 parameter dispersion relation. (a) Logarithmic scale (using a base of 10) of the determinant $|\mathbf{M} - \mathbf{I} e^{-ik2d}|$, for varying angular frequency and Bloch wave number. The SIPs are denoted with red circles. A zoom-in on the right SIP is shown in the inset. (b) Normalized k 's related to the eigenvalues of the transfer matrix \mathbf{M} at a range of frequencies near the SIP. The magenta lines indicate the propagating modes, marked as $\{k_p\}$. The light blue lines indicate the decaying modes, marked as $\{k_d\}$. Black dotted lines and solid lines represent the imaginary and real parts of the normalized wave numbers, respectively.

A stationary point of third order (i.e., an SIP) is characterized by the coalescence of three eigenvalues and three eigenvectors. Figure 3(b) plots the dispersion relation of the structure (normalized complex wave number $\frac{k2d}{\pi}$ vs angular frequency). At each frequency, there are six Bloch modes with six eigenvalues. The magenta lines in Fig. 3(b) indicate propagating modes. The solid magenta lines correspond to the real parts of the eigenvalues, while the dotted ones indicate the imaginary parts. These eigenvalues are purely real, and the real parts of the eigenvalues match exactly the green lines near the SIP in Fig. 3(a). The light blue lines in Fig. 3(b) indicate the nonpropagating (decaying) modes. Similar to the

TABLE I. Two sets of parameters for the studied structure.

Parameter	κ_1	κ_2	κ_3	α	$2d$ (μm)	R (μm)	n_w	n_r
Set 1	0.30	0.16	0.56	0	44	7	2.21	2.21
Set 2	0.20	0.42	0.73	0	20	4	3.42	3.42

propagating modes, the solid and dotted lines indicate the real and imaginary parts of the wave numbers, respectively. Note that there are four decaying modes: two that are complex conjugates. In other words, two modes have eigenvalues with a positive real part, and the other two with a negative real part. From Fig. 3(b) we identify the SIP frequency as the frequency at which three of the wave numbers coalesce into a single real value. It corresponds to the frequency marked by a red circle in Fig. 3(a), $\omega = \omega_s$. Due to reciprocity, two SIPs are obtained (at the same frequency), corresponding to two triply degenerate counterpropagating modes.

We emphasize that an SIP is a condition where both eigenvalues and eigenvectors coalesce. However, Fig. 3(b) only shows the coalescence of the eigenvalues. The coalescence of the eigenvectors is verified through the coalescence parameter that was defined in Refs. [21,22] for the SIP (see Appendix A for details). Appendix A also describes the structure design and optimization process used for obtaining the parameters in Table I. Consequently, it can be inferred that Fig. 3(b) verifies that the marked points in Fig. 3(a) are indeed SIPs, meaning that $\omega_s = \omega_{\text{SIP}}$.

B. Almost-overlapping stationary inflection points

The proposed structure can exhibit SIP dispersion properties in a range of frequencies and locations in the BZ, controlled by the design parameters. Modifying the parameters ($d, R, \kappa_1, \kappa_2, \kappa_3$), depicted in Fig. 1, enables us to generate an SIP in different locations in the dispersion relation. This section considers the set of parameters designated as set 2 in Table I. As in Sec. II A, Fig. 4(a) plots the colormap of the determinant of the matrix: $\mathbf{M} - \mathbf{I} e^{-ik2d}$. Figure 4(b) depicts the Bloch wave numbers of the transfer matrix as a function of frequency. At first glance, it seems that a flat band with zero group velocity is formed at the center of the BZ with wavelength $\lambda \approx 1.55 \mu\text{m}$, represented with a red circle. A zoom-in on the dispersion relation in the red circle is shown in the inset. We define the frequency related to this wavelength as before, ω_s . In a scenario of a flat band, the transfer matrix of the structure should exhibit a degeneracy of six eigenvalues related to $k = 0$. However, the eigenvalues depicted in Fig. 4(b) indicate that this so-called flat band consists, in fact, of two very close SIPs located at both sides of the BZ center. This should not be surprising as it is well known that an intersection of different spectral branches at $k = 0$ is only possible for a one-dimensional periodic structure that exhibits glide plane symmetry [26–29]. However, as the structure depicted in Fig. 1 does not exhibit glide symmetry, the two SIPs cannot fully intersect at the center of the BZ and therefore cannot support degenerate SIPs.

Thus, we understand that the studied structure can support the formation of SIPs over large domains in the BZ, and at different wavelengths. The frequencies and wave numbers of such SIPs can be controlled by modifying and optimizing the set of parameters that describe the structure. In Sec. II A we showed an SIP that is located at $\frac{k2d}{\pi} \approx 0.2$, which makes this SIP separated from its backward propagating counterpart. In this section, we described an SIP that is formed almost at the center of the BZ, at $\frac{k2d}{\pi} \approx 0.05$. This shows that this structure

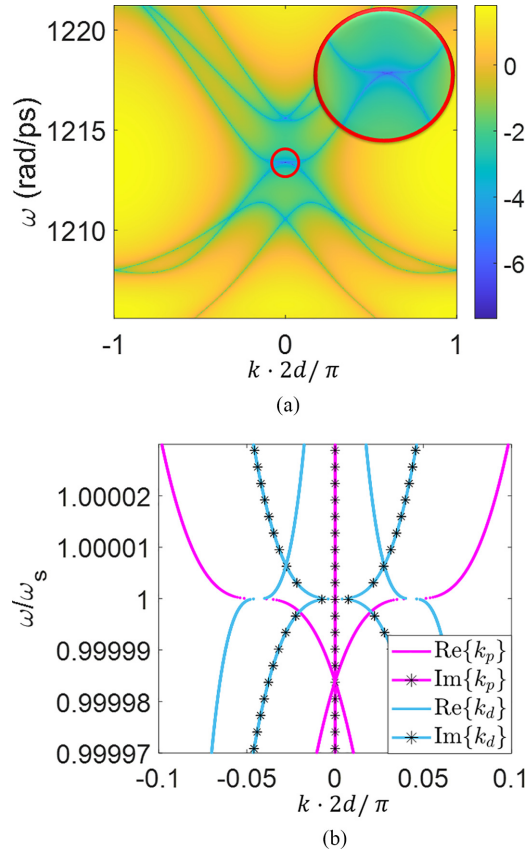


FIG. 4. Set 2 parameter dispersion relation. (a) Logarithmic scale (using base of 10) of the determinant $|\mathbf{M} - \mathbf{I} \cdot e^{-ik \cdot 2d}|$, for varying angular frequency and Bloch wave number. The two close SIPs are marked by the red circle. A zoom-in on the SIPs is shown in the inset. (b) Normalized k 's related to the eigenvalues of the transfer matrix M at a range of frequencies near the SIP. The magenta lines indicate propagating modes, marked as $\{k_p\}$. The light blue lines indicate decaying modes, marked as $\{k_d\}$. Black dotted lines and solid lines correspond to the imaginary and real parts of the normalized wave numbers, respectively.

is incredibly versatile since it can generate SIPs at various locations in the BZ.

III. FINITE LENGTH STRUCTURE

A. Single input–multiple output transmission and reflection

The dispersion relation and frozen mode regimes discussed in Sec. II are obtained only for infinitely long structures. However, any realistic structure is finite in length, thus leading to resonances with optical properties that may differ a bit from those of the infinitely long structure. Resonances in such a realistic finite-length structure may not support a “perfect” frozen light mode. However, as more unit cells are added, the closer the SIP resonance is to the SIP frequency, and the smaller the group velocity is at the resonance. Thus, the longer the structure, the closer the characteristics of the propagating waves in the structure become to those expected at an SIP. Therefore, we expect to obtain enhancement of properties, such as the Q factor, by using finite-length structures with a sufficient number of unit cells.

In order to investigate the transmission and reflection properties of a finite-length structure, we analyze a waveguide with length $l = 2dN$ where N is the number of unit cells. Any resonance response of such structure in the vicinity of an SIP is expected to be enhanced due to the small group velocity. In addition, the larger the number of unit cells, the closer the resonance frequency to the SIP. Recall that the structure consists of three parallel waveguides, (see Fig. 1) with three IO ports. Consequently, the structure can be excited in many ways. We analyze the power transmission and reflection properties, for the case where an input field excites only the upper waveguide (port 3) from the left. We use the transfer-matrix approach to obtain the intensity of the fields exiting from the three left-hand-side waveguides (i.e., reflection) and from the three right-hand-side waveguides (transmission) of the structure. Equation (7) defines the transmission and reflection power, which are denoted as T_m^2 and R_m^2 , respectively. The plus and minus signs indicate forward and backward propagating fields and the subscript m denotes at which port the field is calculated. The number in the brackets is the point on the propagation axes where the field is calculated. Figure 2 shows the port numbers:

$$T_m^2 = \left| \frac{E_m^+(l)}{E_3^+(0)} \right|^2, \quad R_m^2 = \left| \frac{E_m^-(0)}{E_3^+(0)} \right|^2, \quad m = 1, 2, 3. \quad (7)$$

Figure 5(a) shows the transmission and reflection spectra of a finite-length structure with $N = 60$, excited through the upper waveguide input (port 3). In this figure, the SIP frequency obtained for set 1 is designated as ω_{SIP} . It can be seen that the transmitted signal through port 3 and those reflected through ports 1 and 2 exchange power as a function of frequency, while the signals at the other ports are zero. At frequencies around the SIP, the spectral profiles in the transmission and reflection ports become more oscillatory and exhibit narrower peaks. This is clearly seen in Fig. 5(b), which is a zoom-in of T_3^2 [marked in the black rectangle in Fig. 5(a)]. At $\omega \approx 0.999\omega_{\text{SIP}}$, the fast oscillations in the spectral responses stop and a resonance in the reflection from port R_1^2 is formed, accompanied by zero transmission through ports T_3^2 and a complementary decrease in R_2^2 . At ω_{SIP} , all the power is reflected through the lower waveguide (R_1^2). The observed increase in the density of the spectral peaks in the vicinity of the SIP indicates that the group velocity is indeed smaller close to the SIP frequency. It also implies that by introducing optical gain into the structure, it should be possible to obtain large optical amplification and even lasing.

B. Single input–single output transmission port

In order to obtain an SIP, it is necessary for the structure to support at least three modes in each direction, thus necessitating the three-path waveguide arrangement. However, for any practical application such as a high-gain amplifier or laser, it is advantageous to have a single input and two outputs, reflection (from the input port) and transmission from a second port. This can be achieved by closing the IO ports at the end of the (finite) structure as shown in Fig. 6: Input ports 1 and 2 and output ports 2 and 3 are closed by introducing reflectors which can be implemented as distributed Bragg reflectors (DBRs). A DBR is a natural choice for implementing an integrated

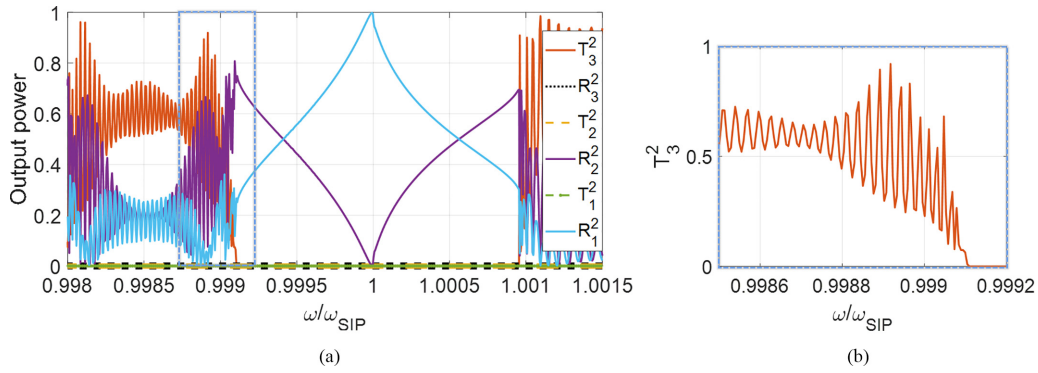


FIG. 5. (a) Transmission and reflection from six ports of a finite-length waveguide structure with 60 unit cells. (b) Transmission from input port 3 to output port 3, near the SIP frequency. The parameters in set 1 are used.

waveguide reflector. In this scenario, we chose the reflectors to exhibit perfect reflectivity. Different DBR designs facilitate high reflectivity as well as control over the reflected spectral band [30,31]. The closed structure possesses two ports which can be considered as IO for optical amplification purposes or two output ports for lasing, similar to a Fabry-Pérot (FP) laser. Consequently, the reflection and transmission ports of the structures are at port 3 (left) and at port 1 (right), respectively. The choice between different waveguides for the IO ports stems from the fact that an SIP formation necessitates coupling between forward and backward propagating waves. The position of the DBRs ensures that the input signal propagates through all the waveguides in both directions. Nevertheless, additional configurations for “closing” the structure (i.e., obtaining single input and single output) are possible. The study of such configurations is beyond the scope of this paper. In this finite-length model, we assume no losses, therefore due to energy conservation the sum of the transmission and the reflection powers equals 1.

Figure 7 plots the transmission spectrum T^2 , for two structure lengths of 30 and 70 unit cells. There are several things to note in the transmission spectrum of the device. The transmission exhibits oscillations similar to a FP cavity [compared to the spectral properties of the “open” structure shown in Fig. 5(a)]. This result is not surprising, since the closing of some of the ports in the structure introduces feedback that couples between forward and backward propagating waves (as in an FP cavity). However, in the vicinity of the SIP frequency, these oscillations corresponding to the FP resonances become dense and sharper (higher Q factor). This is attributed to the slow-light effect in the vicinity of the SIP which effectively reduces the local free spectral range (FSR) of the FP cavity.

The resonances of the structure consisting of $N = 70$ unit cells are denser and sharper than those of the $N = 30$ device. This is due to the longer FP cavity, which, similar to the slow-light effect, reduces the FSR. This effect is particularly strong near the SIP frequency (shown in the inset of Fig. 7), where the resonances of the longer structure are much sharper than those of the shorter one due to the combination of the longer device and slow-light effect.

IV. TOLERANCE TO GEOMETRICAL IMPERFECTIONS

Any realistic structure comprising periodic unit cells is expected to exhibit variations between the unit cells due to fabrication tolerances and errors. Such variations might have a non-negligible impact on the spectral properties of the device and impair its performance. In this section, we present a preliminary study of the impact of fabrication tolerances and errors on the transmission properties of the device analyzed in Sec. III A [see also Fig. 5(a)]. To account for random fabrication errors, we assume that they can be represented as random variations in the structure parameters (coupling coefficients and the radii of the rings). We note that there are additional structure parameters that might be subjected to fabrication tolerances (e.g., the widths and thicknesses of the rings), leading to modification of the device’s spectral properties. Nevertheless, variations in these parameters essentially modify the resonances of the microrings, and, therefore, their impact can be incorporated as effective variations in the rings’ radii. We consider the structure whose ideal spectral response is depicted in Fig. 5(a). As stated in Sec. III A, the structure consists of three transmissions and three reflections, and is composed of 60 unit cells. We model fabrication errors by

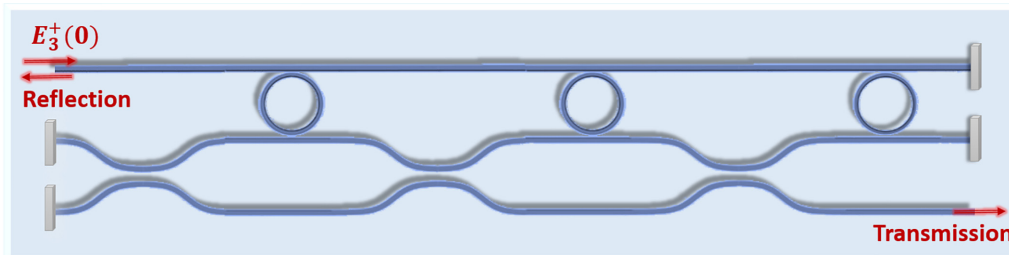


FIG. 6. Finite-length model, closed with reflective mirrors. This arrangement has one input port and one transmission port.

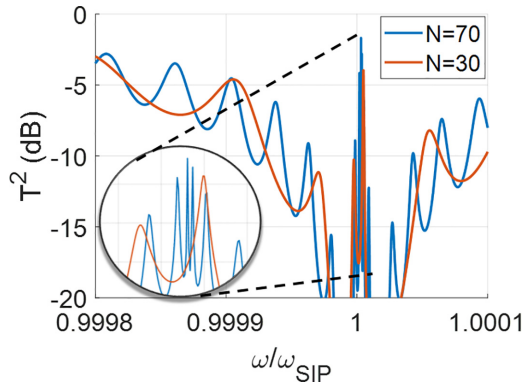


FIG. 7. Transmission of the closed model with mirrors, for 30 and 70 unit cells.

assuming that the coupling coefficients and the radius of the ring in each unit cell follow a Gaussian distribution (the mean being the ideal value). Figure 8(a) depicts an example for the reflected spectral power from port 1, in the vicinity of the SIP frequency obtained for set 1. In this example, the coupling coefficients follow a Gaussian distribution with a standard deviation of 5% of each coefficient value. The microrings' radii are also assumed to exhibit Gaussian distribution with standard deviation (STD) of 3 nm. It can be seen that although the reflection spectrum is noisy, the overall profile is retained, and the main peak of the resonance remains. We repeated this calculation 40 times, using the same Gaussian distribution noted above in order to obtain a statistical overview of the expected spectrum of imperfect structures. For each frequency, we obtained the STD of the reflection power distribution and plotted corresponding error bars in Fig. 8(b). Note that although the variations in the spectrum are noticeable, the main feature of the peak still remains. Analogous conclusions were obtained in Ref. [32] when analyzing the quality factor of DBE resonances, where the standard deviation was growing with the length of the DBE resonator. The present analysis is just an example of the potential impact of imperfections on the performances of a device operating near an SIP. A comprehensive analysis of this topic is beyond the scope of this paper and the results of a detailed study will be published in a separate paper.

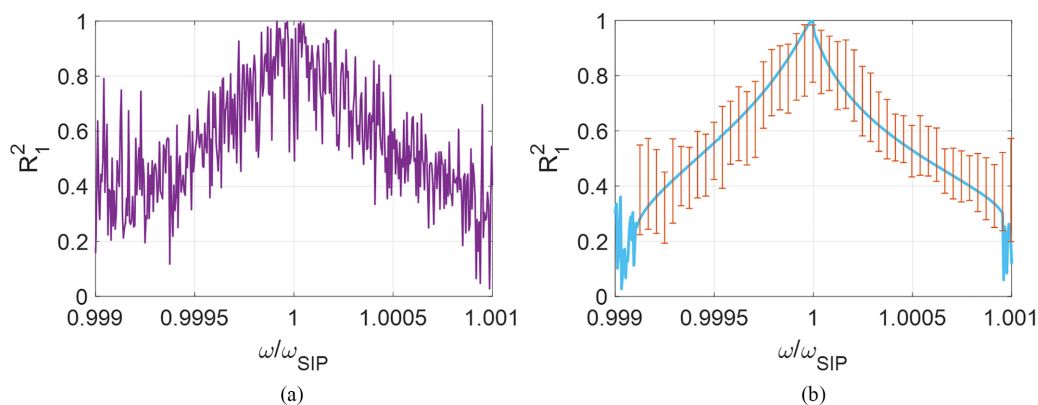


FIG. 8. (a) Reflection from port 1 of a finite-length waveguide structure with 60 unit cells, which has a geometrical error in each unit cell. (b) Reflection from port 1 with error bars representing the standard deviation for each frequency. The parameters in set 1 are used.

V. ANALYZING GAIN PROPERTIES

The sharp resonances associated with a high quality factor and the SIP frequency indicate that such a structure could be useful for the realization of low-threshold lasers [16,24,33]. To identify the lasing threshold of the structure we introduce an imaginary part to the refractive index of the resonators and waveguides, and consider the dependence of the threshold level on the number of unit cells. The lasing condition is a singular point, which is characterized as a pole in the transmission spectral response. In other words, at the lasing threshold, the output power calculated using the transfer matrix approaches infinity regardless of the input intensity level, as shown in Ref. [34], chap. 5. In practice, gain saturation effects, which are often not considered in a linear transfer-matrix analysis, limit the actual output power. Nevertheless, such effects do not affect the lasing threshold.

As the structure supports many resonances that can potentially lase, we consider the resonance which is closest to the SIP frequency because it is the one that retains the SIP properties the most. As the group velocity in the vicinity of this frequency is lowest, the intensity buildup at this frequency is expected to be enhanced substantially and exhibit the lowest threshold level. We continue to focus on the SIP obtained with set 1 parameters. Figure 9(a) depicts the resonance (i.e., the lasing) angular frequency (denoted by magenta dots) as a function of the number of unit cells. The resonance frequency approaches ω_s , which corresponds to ω_{SIP} frequency for the magenta points, as the number of the unit cells increases.

As a comparison, we also calculate the threshold level of a structure exhibiting a RBE of a coupled-resonator optical waveguides (CROW) structure [35] composed of ring resonators with radius $R = 7 \mu\text{m}$ (which is the same as the one in set 1 of Table I here considered) coupled to each other with the coupling coefficient $\kappa_r = \kappa_2$ from set 1. The unit-cell length of the CROW is $l = 4R$, which is smaller than the unit-cell length of our structure. Any realistic structure exhibits losses that should be included in the calculation of the lasing threshold. Thus, we introduce a loss parameter of $\alpha = 0.01$ to the ring resonators, equivalent to a 1% power loss per revolution.

Although the comparison is not perfect, it does allow us to get a better understanding of the lasing properties of a device operating in the vicinity of an SIP. The process of

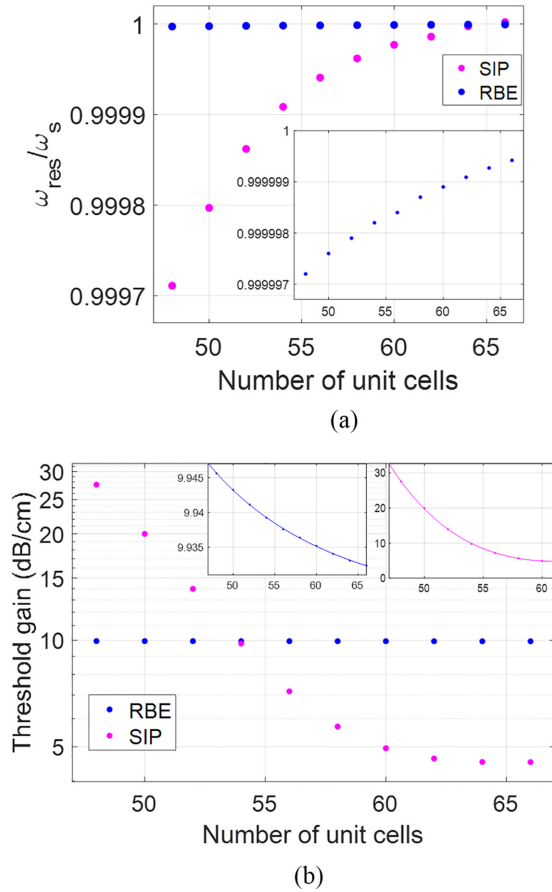


FIG. 9. Dependence of the threshold gain in the waveguides, and the lasing frequency vs the number of unit cells of the structure. (a) The angular resonance frequency ω_{res} , which is the closest to the stationary point ω_s , as a function of the number of unit cells. ω_s refers to the stationary point frequency, either ω_{SIP} (for the magenta dots) or ω_{RBE} (for the blue dots). Magenta points denote change in resonance frequency normalized by the SIP frequency in our structure. Blue points denote change in resonance normalized by the RBE frequency in the CROW. (b) The threshold gain for RBE in the CROW model, and SIP in the proposed model vs the number of unit cells. The y axis is in logarithmic scale. Magenta points denote SIP threshold gain. Blue points denote RBE threshold gain. The two insets show polynomial fitting of the SIP (magenta) and the RBE (blue). Note that the y axis in those figures is in linear scale.

calculating the threshold gain for a finite structure is detailed in Appendix B.

Figure 9(a) also shows the lasing frequency of a CROW structure as a function of the number of unit cells, N (blue dots). The lasing frequencies are normalized to either ω_{SIP} or to ω_{RBE} , according to the relevant structure. Note that in this case $\omega_{\text{RBE}} \approx 1224$ (rad/ps). It can be seen that the number of unit cells N has more impact on the lasing frequency of the SIP supporting structure than on that of the RBE. However, although the lasing frequency of the RBE supporting structure seems to be independent of N , this is not the case. The inset of the figure shows a zoom-in on the lasing frequency of the RBE structure, indicating that it also approaches ω_{RBE} as N increases. In both cases, the dependence of the resonances on N can be described as $\omega_{\text{th}} \propto \alpha + \beta N^{-1} + \gamma N^{-3}$.

Figure 9(b) depicts a comparison between the threshold gain (in the waveguides) near the SIP (in pink) of the structure depicted in Fig. 6, and that corresponding to the RBE in the CROW. The parameters of set 1 in Table I have been used in the comparison. The threshold gain is presented as a function of the number of unit cells in each structure. The scale of the y axis is in logarithmic scale. There are a couple of important points to be noted: first, the lasing threshold gain of the SIP supporting structure decreases rapidly with the number of unit cells, reaching a minimal level of ≈ 4.5 dB/cm at $N = 64$, and second is that the lasing threshold stabilizes for longer structures. We attribute the threshold gain stabilization to the fact that the loss in structure is also proportional to the number of unit cells. Thus, for a sufficiently long structure, this loss mechanism dominates all other mechanisms in the structure (e.g., output coupling loss), and the lasing threshold is obtained when the gain becomes equal to the loss at each unit cell. In contrast, the dependence of the threshold gain on N for the RBE case seems to be approximately constant. However, zooming in on the RBE lasing threshold N dependence [shown as the left inset in Fig. 9(b)] indicates that this is not the case. The threshold gain near the RBE of the CROW is not constant, but rather decreases slowly with N , at a slope that is substantially slower than that of the SIP supporting structure.

Second, by fitting the two calculated curves [see insets of Fig. 9(b)] we find that the threshold gain dependence on N in both cases can be described by a third-order polynomial in N^{-1} : $a + bN^{-1} + cN^{-3}$. This dependence agrees with previous results [6,7,16]. The main difference between the curves is the value of the fitting coefficients b and c corresponding to the dependence on N^{-1} and N^{-3} respectively. In the CROW structure we find that $|b_{\text{RBE}}| \approx 10^{-1}$ dB/cm and $c_{\text{RBE}} \approx 2 \times 10^4$ dB/cm, while in the SIP supporting structure we find that $|b_{\text{SIP}}| \approx 2 \times 10^{-4}$ dB/cm and $c_{\text{SIP}} \approx 2 \times 10^7$ dB/cm. There is a substantial difference (of orders of magnitude) between these coefficients, which has a dramatic impact on the properties of the two stationary points (the SIP and RBE). The decrease of the lasing threshold as a function of N is significantly faster for the structure supporting an SIP. This is seen by the larger fitting coefficient of the N^{-3} term and the smaller coefficient of the N^{-1} term for that structure. Consequently, the dominant dependence of the lasing threshold of the SIP structure and the CROW is N^{-3} and N^{-1} , respectively. It should also be noted that although the threshold value of the SIP structure is larger than that of the CROW for $N < 54$, once the structure length exceeds 54 unit cells, the SIP lasing threshold becomes smaller. Although a direct comparison between the structures is difficult because they are very different from each other, the overall trend indicates the advantages of operating near a SIP. Clearly, a laser operating at an SIP can potentially exhibit a lower lasing threshold than that of conventional lasers.

VI. CONCLUSION

In this paper, we introduced a periodic structure composed of three parallel waveguides that are coupled to each other by ring resonators and directional couplers. We calculated the dispersion relation of the structure by means of the

transfer-matrix method and showed that a proper choice of the structure parameters (coupling coefficients, ring radius, and length of the unit cell) leads to the formation of SIPs in the dispersion relation. We also showed that it is possible to control the frequency and wave number of the SIPs. Moreover, we studied the properties of finite-length structures (i.e., with a finite number of unit cells). We calculated the spectral transmission and reflection at each port and studied their properties in the vicinity of the SIP frequencies. We then studied the transmission and reflection properties of a closed structure, exhibiting only two ports, by introducing reflectors at the other four ports. This is only one of the possibilities of closing such a structure, and other closed-structure configurations might lead to different spectral transmission and reflection. Specifically, we focused on two structures with $N = 30$ and 70 unit cells. We found that longer structures yield sharper resonances exhibiting higher Q factors. We attribute this to the fact that the longer the structure, the closer the resonance gets to the zero-group-velocity point in the dispersion relation. We briefly discussed the impact of imperfections due to fabrication errors and tolerances on the spectral properties of this structure. Finally, we analyzed the ability of this structure to serve as a laser by introducing optical gain into the structure. Specifically, we focused on the dependence of the lasing threshold gain on the number of unit cells, N . We compared the lasing threshold gain at the SIP frequency and that of a structure supporting a second-order stationary point (i.e., RBE). We found that although the dependence of the threshold gain on N is similar in both cases and can be described by a third-order polynomial in N^{-1} , the threshold level of SIP-supporting structure decreases faster with increasing N . Thus, we conclude that this structure is highly attractive for low-threshold laser devices.

ACKNOWLEDGMENT

This paper is based upon work supported by AFOSR Grants No. FA8655-20-1-7052 and No. FA9550-18-1-0355.

APPENDIX A: OPTIMIZATION PROCESS

This Appendix describes the design and optimization process of the SIP-supporting structure. For this design, there are five independent parameters that need to be determined (and optimized): the power coupling coefficients ($\kappa_1, \kappa_2, \kappa_3$), the ring radius (R), and a length parameter, which is related to the length of the unit cell (d). There is an additional degree of freedom, which is the position of the directional coupler (in the longitudinal direction) between the middle and the lowest waveguide. Here, we choose to position it at the center of the unit cell, equally distanced from the two microrings. Nevertheless, this is just a specific choice. Changing the position of the directional coupler breaks mirror symmetry, in the z direction inside the unit cell, which might allow us to get another SIP because it is a nonsymmetric stationary point. This structure does not exhibit any symmetry in the vertical axes, which is a requirement for obtaining an SIP.

Since there are many parameters that need to be determined, a numerical optimization approach is required. To determine the design parameters we minimize the coalescence

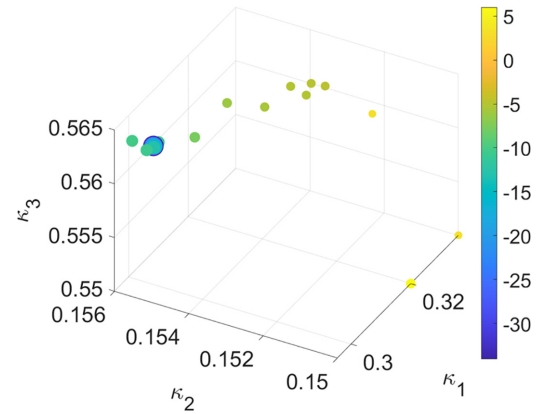


FIG. 10. Convergence of the optimization process. The x , y , and z axes denote the intensity coupling coefficients. The size of the dots and their color indicate the value of D_h in dB. The bigger and darker the dots are the smaller D_h is.

parameter in Eq. (A1), introduced in Ref. [36]. This parameter quantifies the degree of coalescence between a number of complex vectors, determined by the order of the stationary point S_0 . For example, in the case of an SIP, the degree of coalescence of three eigenvectors of the transfer matrix $\{\phi_k\}$, having the same eigenvalue, is minimized. When the angles between all of the eigenvectors approach zero (i.e., all the eigenvectors are parallel), the coalescence parameter approaches zero as well, i.e., $D_h \rightarrow 0$. At the start of the optimization process, the length of the unit cell and the radius of the microring are chosen randomly. The coupling coefficients are then varied manually by means of trial and error until a potential SIP is formed in the dispersion relation at a certain wavelength λ_p . Then, the coupling coefficients are optimized numerically in an attempt to minimize D_h for the wavelength λ_p . Here we employ the Nelder-Mead simplex algorithm for the optimization [37]. Our objective function is $f(\{\phi_k\}) = D_h(\{\phi_k\}) + 10^2[\mathcal{D}(\gamma) - \mathcal{D}_{\text{desired}}]$. The term D_h corresponds to the coalescence parameter of a group of eigenvectors having the same eigenvalue γ . The “degeneracy” parameter corresponds to the degeneracy (i.e., algebraic multiplicity) of the eigenvalue γ , related to the group of eigenvectors $\{\phi_k\}$. The $\mathcal{D}_{\text{desired}}$ parameter is the desired order of the degeneracy of the eigenvalue γ (e.g., $\mathcal{D}_{\text{desired}} = 3$ for an SIP). Therefore, the use of this objective function favors the formation of $\mathcal{D}_{\text{desired}}$ identical eigenvectors and eigenvalues:

$$D_h = \frac{1}{\binom{S_0}{2}} \sum_{\substack{m=1, n=1 \\ m > n}}^{S_0} \sin(\theta_{n,m}), \quad \cos(\theta_{n,m}) = \frac{\langle \phi_n | \phi_m \rangle}{\|\phi_n\| \|\phi_m\|}. \quad (\text{A1})$$

Figure 10 depicts the convergence of the optimization process that yielded the coupling coefficients of set 1. In this case, λ_p is the wavelength of the SIP $\lambda \approx 1.54 \mu\text{m}$, and the ring radius and the unit-cell length are defined in Table I. The dots in the figure indicate the position in the three-dimensional coupling coefficients space $\{\kappa_1, \kappa_2, \kappa_3\}$ of the structure during the optimization process. The size and the color of the dots indicate the value of the coalescence parameter. The small yellow dot located at $\{\kappa_1, \kappa_2, \kappa_3\} = \{0.32, 0.15, 0.55\}$ indicates D_h in the initial point (obtained manually as described

above) of the optimization process. At this point, $D_h > 0.3$, indicating that the eigenvectors have not coalesced yet. The dots show the progress of the optimization process, indicating the trajectory in the coupling coefficients space and the corresponding coalescence parameter. At the end of the process we get $D_h \approx -30$ dB [dB stands for $10 \log_{10}(D_h)$].

APPENDIX B: CALCULATING THE THRESHOLD GAIN

In this Appendix, we present the process for calculating the threshold gain level and the resonance frequency for a finite-length structure with single input and transmission ports, as depicted in Fig. 6. A uniformly distributed gain is added to the structure, by introducing an imaginary part (n_i) to the refractive index of the waveguides and the ring resonators. First, we find the amplitude transmission of the structure as a function of the frequency and gain. We then plot the absolute value of the amplitude transmission $\log_{10}|T^2|$ as a function of these parameters, as depicted in Fig. 11 for a structure composed of 56 unit cells (in logarithmic scale). This plot allows for the identification of the resonance (i.e., lasing) frequencies *and* their corresponding lasing thresholds. A threshold condition corresponds to a pole in the transmission function, which is manifested as a peak in the transmission function. Next, we identify the resonance frequency closest to the SIP frequency (the SIP frequency was obtained by using the optimization process described in Appendix A). While the resonance frequency does not coincide with the SIP

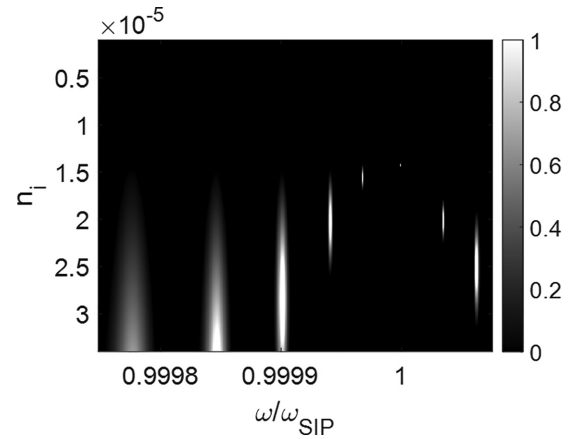


FIG. 11. Log scale of the transmission power for a finite-length structure with 56 unit cells, and single input port and transmission port. The transmission is plotted as a function of the angular frequency and the imaginary part of the effective refractive index of a uniform (single mode) waveguide. Three lasing conditions are visible as the narrow frequency sharp peaks.

frequency, it approaches it for a very large number of unit cells, i.e., $\omega_{\text{res}} \xrightarrow{N \rightarrow \infty} \omega_{\text{SIP}}$ [5]. The gain level at which the transmission is maximal is the threshold gain of the structure at the relative resonance (i.e., lasing) frequency. The lasing threshold is identified as the gain at which the transmission is maximal at the resonance frequency of interest.

- [1] K. Kiyota, T. Kise, N. Yokouchi, T. Ide, and T. Baba, Various low group velocity effects in photonic crystal line defect waveguides and their demonstration by laser oscillation, *Appl. Phys. Lett.* **88**, 201904 (2006).
- [2] S. Ek, P. Lunnemann, Y. Chen, E. Semenova, K. Yvind, and J. Mork, Slow-light-enhanced gain in active photonic crystal waveguides, *Nat. Commun.* **5**, 5039 (2014).
- [3] N. A. Mortensen and S. Xiao, Slow-light enhancement of Beer-Lambert-Bouguer absorption, *Appl. Phys. Lett.* **90**, 141108 (2007).
- [4] B. S. Song, S. Noda, T. Asano, and Y. Akahane, Ultra-high-q photonic double-heterostructure nanocavity, *Nat. Mater.* **4**, 207 (2005).
- [5] H. Noh, J.-K. Yang, I. Vitebskiy, A. Figotin, and H. Cao, Giant resonances near the split band edges of two-dimensional photonic crystals, *Phys. Rev. A* **82**, 013801 (2010).
- [6] M. Y. Nada, M. A. K. Othman, and F. Capolino, Theory of coupled resonator optical waveguides exhibiting high-order exceptional points of degeneracy, *Phys. Rev. B* **96**, 184304 (2017).
- [7] A. Figotin and I. Vitebskiy, Slow wave phenomena in photonic crystals, *Laser Photonics Rev.* **5**, 201 (2011).
- [8] A. Figotin and I. Vitebskiy, Slow light in photonic crystals, *Waves in Random and Complex Media* **16**, 293 (2006).
- [9] N. Gutman, C. Martijn de Sterke, A. A. Sukhorukov, and L. C. Botten, Slow and frozen light in optical waveguides with multiple gratings: Degenerate band edges and stationary inflection points, *Phys. Rev. A* **85**, 033804 (2012).
- [10] H. Li, I. Vitebskiy, and T. Kottos, Frozen mode regime in finite periodic structures, *Phys. Rev. B* **96**, 180301(R) (2017).
- [11] W. Tuxbury, R. Kononchuk, and T. Kottos, Non-resonant exceptional points as enablers of noise-resilient sensors, *Commun. Phys.* **5**, 210 (2022).
- [12] H. Hodaei, A. U. Hassan, S. Wittek, H. Garcia-Gracia, R. El-Ganainy, D. N. Christodoulides, and M. Khajavikhan, Enhanced sensitivity at higher-order exceptional points, *Nature (London)* **548**, 187 (2017).
- [13] N. Habler and J. Scheuer, Higher-order exceptional points: A route for flat-top optical filters, *Phys. Rev. A* **101**, 043828 (2020).
- [14] J. Scheuer, D. Filonov, T. Vosheva, and P. Ginzburg, Extraordinary broadband impedance matching in highly dispersive media—the white light cavity approach, *Opt. Express* **30**, 5192 (2022).
- [15] B. Paul, N. K. Nahar, and K. Sertel, Frozen mode in coupled silicon ridge waveguides for optical true time delay applications, *J. Opt. Soc. Am. B* **38**, 1435 (2021).
- [16] A. Herrero-Parareda, N. Furman, T. Mealy, R. Gibson, R. Bedford, I. Vitebskiy, and F. Capolino, Lasing at a stationary inflection point, *Opt. Mater. Express* **13**, 1290 (2023).
- [17] T. Baba and D. Mori, Slow light engineering in photonic crystals, *J. Phys. D* **40**, 2659 (2007).
- [18] M. D. Lukin and A. Imamogulu, Controlling photons using electromagnetically induced transparency, *Nature (London)* **413**, 273 (2001).

- [19] M. M. Kash, V. A. Sautenkov, A. S. Zibrov, L. Hollberg, G. R. Welch, M. D. Lukin, Y. Rostovtsev, E. S. Fry, and M. O. Scully, Ultraslow group velocity and enhanced nonlinear optical effects in a coherently driven hot atomic gas, *Phys. Rev. Lett.* **82**, 5229 (1999).
- [20] N. Furman, T. Mealy, M. S. Islam, I. Vitebskiy, R. Gibson, R. Bedford, O. Boyraz, and F. Capolino, Frozen mode regime in an optical waveguide with a distributed Bragg reflector, *J. Opt. Soc. Am. B* **40**, 966 (2023).
- [21] M. Y. Nada, T. Mealy, and F. Capolino, Frozen mode in three-way periodic microstrip coupled waveguide, *IEEE Microwave Wireless Compon. Lett.* **31**, 229 (2020).
- [22] A. Herrero-Parareda, I. Vitebskiy, J. Scheuer, and F. Capolino, Frozen mode in an asymmetric serpentine optical waveguide, *Adv. Photonics Res.* **3**, 2100377 (2022).
- [23] F. Yazdi, M. A. K. Othman, M. Veysi, A. Figotin, and F. Capolino, A new amplification regime for traveling wave tubes with third-order modal degeneracy, *IEEE Trans. Plasma Sci.* **46**, 43 (2018).
- [24] M. Veysi, M. A. K. Othman, A. Figotin, and F. Capolino, Degenerate band edge laser, *Phys. Rev. B* **97**, 195107 (2018).
- [25] H. Ramezani, S. Kalish, I. Vitebskiy, and T. Kottos, Unidirectional lasing emerging from frozen light in nonreciprocal cavities, *Phys. Rev. Lett.* **112**, 043904 (2014).
- [26] A. Hessel, M. H. Chen, R. C. Li, and A. A. Oliner, Propagation in periodically loaded waveguides with higher symmetries, *Proc. IEEE* **61**, 183 (1973).
- [27] O. Quevedo-Teruel, Q. Chen, F. Mesa, N. J. G. Fonseca, and G. Valerio, On the benefits of glide symmetries for microwave devices, *IEEE J. Microwaves* **1**, 457 (2021).
- [28] C. M. Patil, G. Arregui, M. Mechlenborg, X. Zhou, H. Alaeian, P. D. García, and S. Stobbe, Observation of slow light in glide-symmetric photonic-crystal waveguides, *Opt. Express* **30**, 12565 (2022).
- [29] A. Tamayo-Dominguez, J.-M. Fernandez-Gonzalez, and O. Quevedo-Teruel, One-plane glide-symmetric holey structures for stop-band and refraction index reconfiguration, *Symmetry* **11**, 495 (2019).
- [30] S. Thomas, and S. W. Pang, Dry etching of horizontal distributed Bragg reflector mirrors for waveguide lasers, *J. Vac. Sci. Technol. B* **14**, 4119 (1996).
- [31] M. W. Pruessner, T. H. Stievater, and W. S. Rabinovich, In-plane microelectromechanical resonator with integrated Fabry-Pérot cavity, *Appl. Phys. Lett.* **92**, 081101 (2008).
- [32] M. Y. Nada, M. A. K. Othman, O. Boyraz, and F. Capolino, Giant resonance and anomalous quality factor scaling in degenerate band edge coupled resonator optical waveguides, *J. Lightwave Technol.* **36**, 3031 (2018).
- [33] M. A. K. Othman, F. Yazdi, A. Figotin, and F. Capolino, Giant gain enhancement in photonic crystals with a degenerate band edge, *Phys. Rev. B* **93**, 024301 (2016).
- [34] T. Numai, *Fundamentals of Semiconductor Lasers* (Springer, New York, 2004).
- [35] J. K. S. Poon, J. Scheuer, S. Mookherjea, G. T. Paloczi, Y. Huang, and A. Yariv, Matrix analysis of microring coupled-resonator optical waveguides, *Opt. Express* **12**, 90 (2004).
- [36] A. F. Abdelshafy, M. A. Othman, D. Oshmarin, A. T. Almutawa, and F. Capolino, Exceptional points of degeneracy in periodic coupled waveguides and the interplay of gain and radiation loss: Theoretical and experimental demonstration, *IEEE Trans. Antennas Propag.* **67**, 6909 (2019).
- [37] J. C. Lagarias, J. A. Reeds, M. H. Wright, and P. E. Wright, Convergence properties of the Nelder-Mead simplex method in low dimensions, *SIAM J. Optim.* **9**, 112 (1998).